High-resolution imaging of supraglacial hydrological features on the Greenland Ice Sheet with NASA's Airborne Topographic Mapper (ATM) instrument suite

Michael Studinger[1], Serdar S. Manizade[2,3], Matthew A. Linkswiler[2,3], and James K. Yungel[2,3]

[1]NASA Goddard Space Flight Center, Greenbelt, MD 20771, USA
[2]Science Systems and Applications, Inc., Lanham, MD 20706, USA
[3]NASA Wallops Flight Facility, Wallops Island, VA, USA

Correspondence to: Michael Studinger (michael.studinger@nasa.gov)

Abstract. Seasonal meltwater pools on the surface of the Greenland Ice Sheet (GrIS) during late Spring and Summer in lakes on the surface and transforms the ice sheet's surface into a wet environment in the ablation zone below the equilibrium line. These supraglacial lakes in topographic lows on the ice surface are connected by a dendritic pattern of meandering streams and channels that together form a hydrological system consisting of supra-, en-, and subglacial components. Here, we use lidar data from NASA's Airborne Topographic Mapper (ATM) instrument suite and high-resolution optical imagery collected as part of Operation IceBridge (OIB) in Spring 2019 over the GrIS to develop methods for the study of supraglacial hydrological features. While airborne surveys have a limited temporal and spatial coverage compared to imaging spaceborne sensors, their high footprint density and high-resolution imagery reveal a level of detail that is currently not obtainable from spaceborne measurements. The accuracy and resolution of airborne measurements complement spaceborne measurements, can support calibration and validation of spaceborne methods, and provide information necessary for high-resolution process studies of the supraglacial hydrological system on the GrIS that currently cannot be achieved from spaceborne observations alone.

1 Introduction

During the summer months seasonal surface melting on the Greenland Ice Sheet (GrIS) produces meltwater near the margins of the ice sheet that pools in supraglacial lakes in depressions on the ice surface and forms a dendritic pattern of meandering streams and rivers in the ablation zone below the equilibrium line (e.g., Chu, 2014; Nienow et al., 2017; Pitcher and Smith, 2019, and references therein). The lakes appear as sapphire-blue features to the eye and in natural color imagery (Flowers, 2018) (Fig. 1). The supraglacial streams and channels often connect several lakes and form a hydrological network on the surface of the GrIS that is part of a hydrological system consisting of supra-, en-, and subglacial components (e.g., Chu, 2014; Nienow et al., 2017; Pitcher and Smith, 2019, and references therein). The formation, retention, and drainage of meltwater impacts ice sheet mass balance and therefore ice sheet stability. Over the past decades, runoff from seasonal

30 meltwater production has exceeded ice loss from ice discharge and basal melting at the grounding lines and has become the dominant mechanism of mass loss for the GrIS (Enderlin et al., 2014; van den Broeke et al., 2016). More recently, supraglacial lakes and channels have also been catalogued on the West Antarctic Ice Sheet (Corr et al., 2022).

Several approaches have been used in recent years to study the supraglacial hydrological network of lakes and streams at various spatial and temporal scales. On an ice-sheet-wide scale the network of supraglacial hydrological features and their

35 temporal evolution can be observed with panchromatic, natural color, and multi-spectral imagery available from multiple satellite missions at various spatial resolutions (e.g., Box and Ski, 2007; Pope et al., 2016; Sneed and Hamilton, 2007; Sneed and Hamilton, 2011; Yang and Smith, 2016; Yang et al., 2017, and references therein). Pixel-based surface classification of satellite imagery is a powerful tool for identifying and mapping networks of supraglacial lakes and streams, however, challenges remain with precise spatial registration of repeat high-resolution imagery (e.g., Yang et al., 2017). Estimating

40 water depths from satellite imagery based on reflectance-depth relationships (i.e., optical depth) requires either natural color or multi-spectral imagery (e.g., Pope et al., 2016). Sneed and Hamilton (2011) list several simplifying assumptions necessary for optical depth-based estimates including a homogenous and smooth lake surface without any wind-induced waves and a homogenous lake bottom that is roughly parallel to the lake surface. As shown later in this paper (Fig. 7a) surface waves are not uncommon, and an oblique aerial photograph of a supraglacial lake shows that newly formed thin ice and snow-covered

45 lake ice further complicate depth estimates based on reflectance (Fig. 1). The photograph also shows a complex lake bottom topography and reflectance that is far from homogenous. Dark lake bottom sediments in the form of cryoconite as well as meltwater channels and bottom crevasses can be seen complicating the analysis, although Pope et al. (2016) developed a method that accounts for the presence of cryoconite. Yang and Smith (2013) emphasize the need to gain a better understanding of supraglacial streams which is currently hindered because their relatively narrow width (~1-30 m) makes

50 them undetectable in moderate resolution satellite imagery. However, recent availability of high-resolution satellite imagery shows improvements in our knowledge of supraglacial streams (Yang and Smith, 2013). Whereas small-scale streams several meters wide can be detected with high-resolution satellite imagery, determining their depths from spaceborne measurements remains difficult (Flowers, 2018).
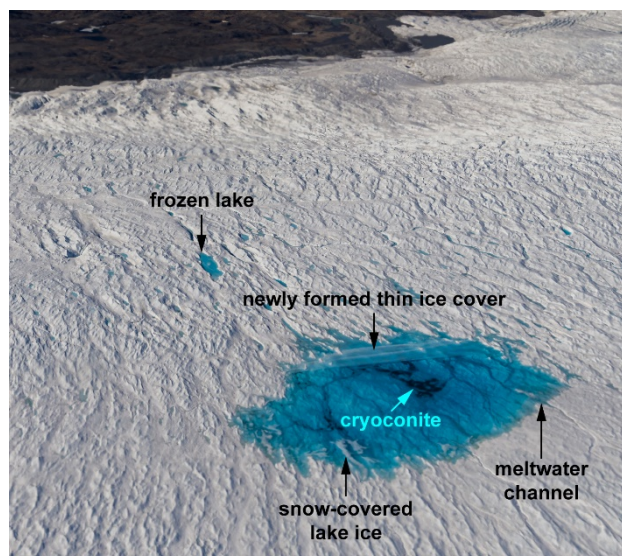
Figure 1: Oblique aerial photograph of a supraglacial lake (approximate location 49° 54' 46" W, 67° 12' 38" N) on Isunnguata Sermia near Kangerlussuaq from May 13, 2019 (Photo: M. Studinger). The lake is approximately 280 m wide. For location see Fig. 2. Surface temperature and surface melt indicator from the Moderate Resolution Imaging Spectroradiometer (MODIS) (Hall et al., 2018; Hall and DiGirolamo, 2019) as well as number of melt days for this location are shown in Fig. A1a.

On a local scale, remotely controlled drone boats and zodiacs equipped with spectroradiometers, digital fathometers, and sonars have been used to measure spectral properties of lakes and streams for calibration and validation of depth estimates based on satellite imagery as well as directly measure water depth (e.g., Box and Ski, 2007; Das et al., 2008; Legleiter et al., 2014; Pope et al., 2016; Smith et al., 2017`; Tedesco and Steiner, 2011).

More recently, spaceborne and airborne lidars have been used to estimate lake depths (Datta and Wouters, 2021; Fair et al., 2020). Airborne measurements can map supraglacial hydrological features on the GrIS at a level of detail that can currently not be accomplished by spaceborne instruments. Airborne measurements can also map supraglacial hydrological features at a spatial scale that cannot be achieved by *in-situ* measurements from short-range drones operated out of remote field camps often requiring line-of-sight communication. More detailed studies of the supraglacial fluvial system on the Greenland Ice Sheet are needed (Smith et al., 2015, p.1001). Here, we use airborne laser altimetry and high-resolution optical imagery collected as part of Operation IceBridge (OIB) in Spring 2019 over the GrIS (MacGregor et al., 2021) to develop methods that allow the study of supraglacial hydrological features currently not possible from space or on the ground.

2 Data sets

OIB campaigns were scheduled to survey the sea ice maximum in March and survey the GrIS at the end of the winter season in early Spring when ice temperatures are still cold to optimize penetration and quality of the ice-penetrating radar data (MacGregor et al., 2021). As a result of this data acquisition strategy some of the campaigns barely captured the early onset of the summer melt in central and southern Greenland, but did not capture the peak of the melt season. In addition to the

Spring campaigns several "summer campaigns" have been flow at the end of the Arctic summer to capture the extent of the summer melt. Because of the timing of these campaigns, temperatures were often below freezing and most of the supraglacial hydrological features were already frozen over. Figure A1 shows the daily mean surface temperature from the Moderate Resolution Imaging Spectroradiometer (MODIS) and the surface melt indicator for the locations of the lakes and
80   channels shown in Figs. 1 and 7-9 (Hall et al., 2018; Hall and DiGirolamo, 2019). We analyze 9 flights from OIB's 2019 Arctic Spring campaign between May 5, 2019 and May 16, 2019 and 4 flights of the Arctic Fall campaign between September 10, 2019 and September 14, 2019 which cover the region where supraglacial hydrological features in the Spring campaign are present (Fig. 2). The 4 flights in September 2019 did not conclusively show the presence of liquid water surfaces and therefore no examples of those flights are discussed in this paper, which primarily focuses on method
85   development. All airborne data used in this study is freely available at the National Snow and Ice Data Center (NSIDC).
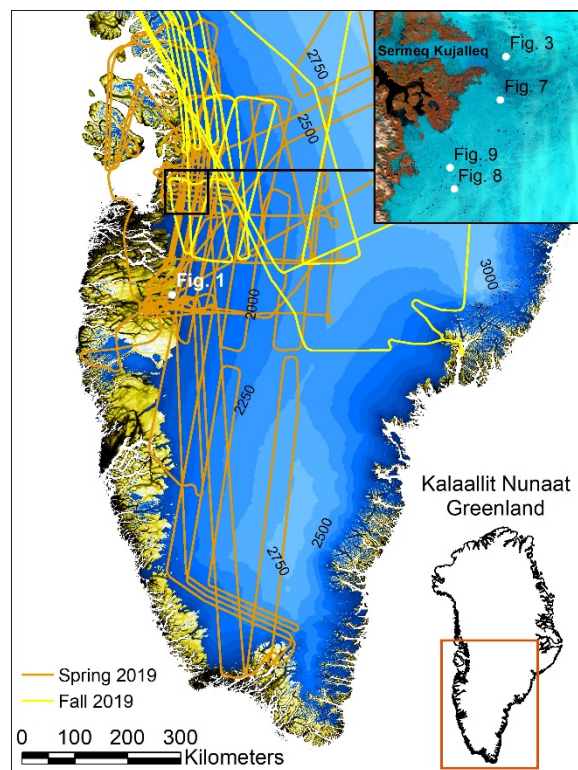
Figure 2. Location map with Spring and Fall 2019 flight lines. Ice surface elevation is shown in blue with a 250 m elevation contour interval. Topography and ice mask data are from the Greenland Ice Mapping Project (GIMP) Digital Elevation Model (Howat et al., 2014) and Morlighem (2021, updated 2021). Inset map over the Sermeq Kujalleq (Jakobshavn Isbræ) region showing figure locations is a
90   Sentinel-2A false color image (bands 11, 8A and 4) from May 17, 2019.

2.1 Airborne Topographic Mapper (ATM) laser altimeters

The ATM instrument suite contains two conically-scanning laser altimeters (lidars) that independently measure the surface elevation along the path of the aircraft at 15° and 2.5° off-nadir angle, respectively (Krabill et al., 2002; MacGregor et al.,

2021; Studinger et al., 2020). At a nominal flight elevation of 460 m above ground level (AGL), the swath widths on the
95   ground are 245 and 40 m, respectively (MacGregor et al., 2021). The 15° wide scanner (ATM T6) transmits at 532 nm
wavelength and the 2.5° narrow scanner (T7) transmits at 532 and 1064 nm with co-located green and infrared footprints.
Both lasers have a pulse repetition frequency of 10 kHz with a 1.3 ns pulse width (MacGregor et al., 2021; Studinger, 2018,
updated 2020). The diameter of the laser footprint on the surface is ~64 cm at 460 m AGL.

We use both the Level 1B geolocated point cloud spot elevation measurements for faster detection of supraglacial
100   hydrological features and the much larger Level 1B waveform data product for bathymetry estimates. Table 1 provides a
summary of the data sets used.

Table 1: Summary of ATM lidar data products used.

Instrument	Off-nadir scan angle	Wavelength	Swath width at 460 m AGL	Contents	NSIDC data set identifier
ATM 6a-T6	15°	532 nm	245 m	Point cloud spot elevation measurements	ILATM1B
ATM 6a-T6	15°	532 nm	245 m	Elevation triplets with waveforms	ILATMW1B
ATM 6d-T7	2.5°	532 nm	40 m	Point cloud spot elevation measurements	ILNSA1B
ATM 6d-T7	2.5°	532 nm	40 m	Elevation triplets with waveforms	ILNSAW1B

2.2 ATM natural color imagery

105   ATM's Continuous Airborne Mapping by Optical Translator (CAMBOT) instrument is a three-channel, natural color, red,
green, and blue (RGB) digital camera with 4896 × 3264 pixels and a 28 mm lens. At a nominal flight elevation of 460 m
AGL, geolocated and orthorectified images span 430 m across track and 290 m along track with a pixel resolution of 7 × 7
cm (MacGregor et al., 2021; Studinger and Harbeck, 2019).

We use both CAMBOT Level 0 raw data (Studinger and Harbeck, 2020) for faster detection of supraglacial hydrological
110   features, and the much larger Level 1B geolocated and orthorectified CAMBOT data product (Studinger and Harbeck,
2019), for analysis of the lidar data. Raw images are collected at 2 Hz and geolocated data products are provided at 1 Hz,
giving sufficient overlap between images at the nominal ground speed of 140 m/s for ATM surveys (MacGregor et al., 2021;
Studinger and Harbeck, 2019).

3 Automatic identification of supraglacial hydrological features

115   We use the normalized difference water index modified for ice (NDWI$_{ice}$) from Yang and Smith (2013) that increases
spectral contrast between liquid water and snow and ice surfaces. The NDWI$_{ice}$ is defined as:

$$\text{NDWI}_{\text{ice}} = \frac{\text{blue} - \text{red}}{\text{blue} + \text{red}} \tag{1}$$

We calculate the NDWI$_{ice}$ from CAMBOT RGB images using the blue and red channels. If 10% of the pixels within a CAMBOT frame exceed an NDWI$_{ice}$ threshold of 0.05 we mark that frame as containing a hydrological feature for analysis

120 (Fig. 3). We use a Sentinel-2 image mosaic from MacGregor et al. (2020) from August 2019 to delineate the maximum melt and lake extent in 2019 by visual inspection (Fig. 6). We form a spatial mask using this extent to bound the search for hydrological features in the airborne data from May 2019. Whereas meltwater also forms upstream in the catchment areas above the equilibrium line, it primarily pools in lakes and streams below the equilibrium line. We use the approximate elevation of the equilibrium line in the August 2019 Sentinel-2 mosaic as a conservative cut-off elevation mask for

125 identifying hydrological features in airborne data from May 2019. We limit the analysis to CAMBOT images within the melt extent mask and inside the grounded ice mask from Howat et al. (2014) to speed up the feature detection.
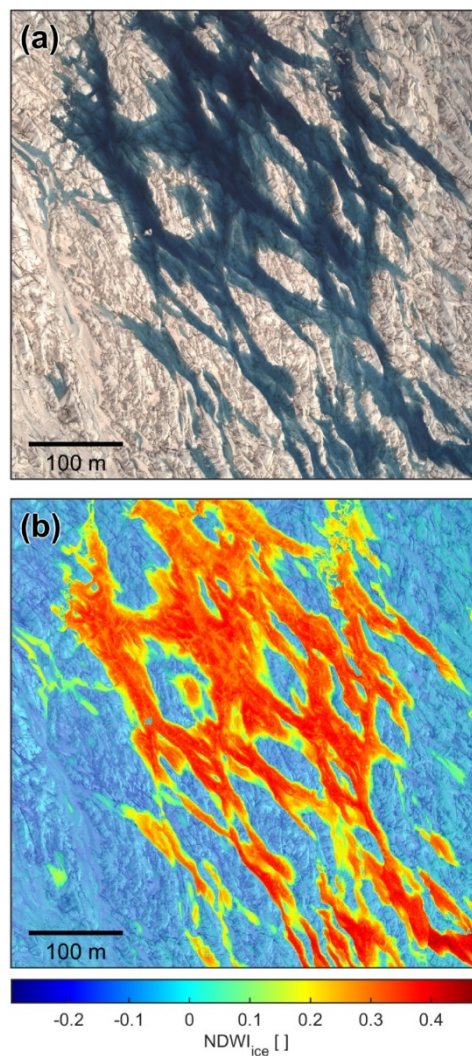
Figure 3. (a) Mosaic of 3 geolocated, orthorectified CAMBOT natural color images of water-filled crevasses on Sermeq Kujalleq (Jakobshavn Isbræ) on May 15, 2019. **(b)** $NDWI_{ice}$ plotted over CAMBOT image mosaic with $NDWI_{ice}$ pixels below the detection
130   threshold of 0.05 shown at 50% opacity/transparency. For location see Fig. 2.

Using a simple $NDWI_{ice}$ threshold can result in false detections. Dark shadows from elevated topography near the ice margin and shadows in deeply incised crevasses and channels can produce $NDWI_{ice}$ values above the detection threshold. More sophisticated, multi-sensor algorithms could be developed to exclude false detections, by using, for example, information from the lidar receiver. However, a more complex classification algorithm would be more computationally expense than the
135    $NDWI_{ice}$ method. The bathymetry algorithm described next detects surface and subsurface returns in the lidar data and distinguishes accurately between snow and ice surfaces and hydrological features that have a finite water depth. Therefore, false detections based on $NDWI_{ice}$ alone will automatically be eliminated during the lidar analysis. The robustness of the hydrological feature identification is suitable for the purpose of this paper, since the goal is not to perfectly delineate hydrological features, but to identify lidar granules for analysis.

4 Estimating lake and stream bathymetry: methods
140

The dielectric contrast between the air-water (lake surface) and the water-ice (lake bottom) interfaces causes reflections of laser energy that can be detected as distinct return pulses. The two-way travel time difference between the lake surface and lake bottom can be used to estimate the depth of hydrological features. The ATM tracking algorithm used for the Level 1B data products is optimized to determine consistent and accurate surface elevations. The ATM tracking algorithm uses 15% of
145   the maximum amplitude above the baseline as a threshold to determine the centroid of a pulse (Fig. 4a). For overlapping lake surface and bottom return pulses the centroid-based tracker returns an averaged slant range between the surface and bottom of the lake (Fig. 4a). To properly track the surface and bottom returns for overlapping pulses, we use dual-peak Gaussian waveform fitting implemented in a nonlinear regression with seven model parameters. We use MATLAB®'s signal processing toolbox to detect local maxima in the waveforms and use these estimates as initial values as input for the
150   nonlinear regression (Appendix B and Fig. 4b).
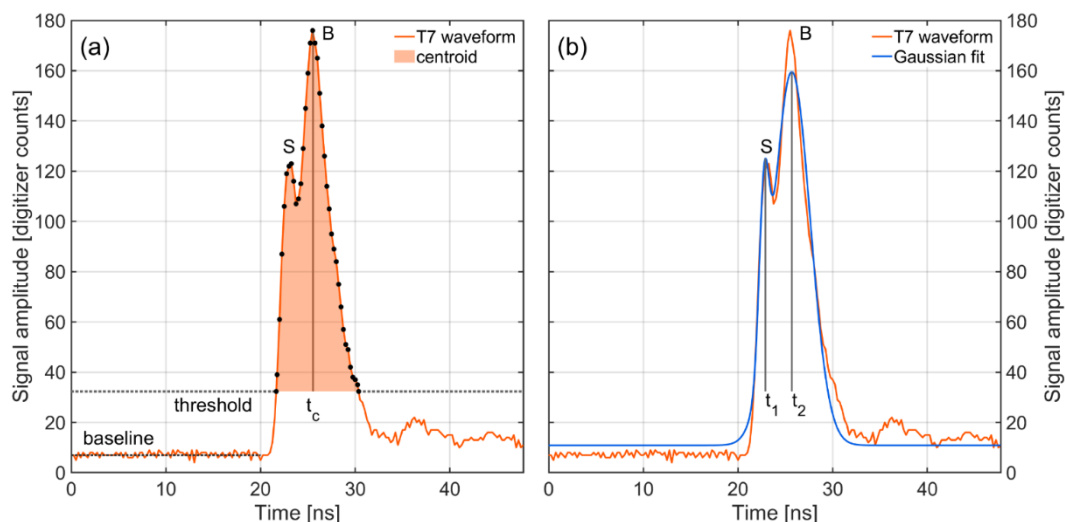
Figure 4: (a) Centroid estimate (t_c) of overlapping surface (S) and bottom (B) return pulses. The centroid-based tracker returns an averaged slant range between the surface and bottom of the lake which in this case is close to the bottom return given the larger amplitude of the bottom return. **(b)** Gaussian fit of two peaks of overlapping surface (S) and bottom (B) return pulses. The slant range in water between the surface and bottom return pulses t_1 and t_2 is 33 cm.

Over hydrological features, there are several cases that need to be considered in estimating water depth. First, it needs to be determined if a laser shot contains a return pulse from both the surface and the bottom. For some cases the return from the surface is stronger (Fig. 5a), for other cases the return from the bottom is stronger (Fig. 5b). For very shallow water depths the surface and bottom returns are typically overlapping (Fig. 5c). For some laser shots there is only a single return which could either be from the lake surface or the much brighter lake bottom or an overlapping surface and bottom return that are so close they appear as a single pulse (Fig. 5d). The algorithm also needs to exclude false pulse detections that are instrument artifacts. The pulses in Fig. 5d are caused by characteristics of the photomultiplier detectors and various other system components such as optical delay fibers and are common in waveform data of airborne and spaceborne lasers (Figs. A2 and A3). The occurrence of these pulses from electronic ringing is consistent in both delay time and percentage of maximum amplitude of the main pulse, and therefore they can reliably be excluded.
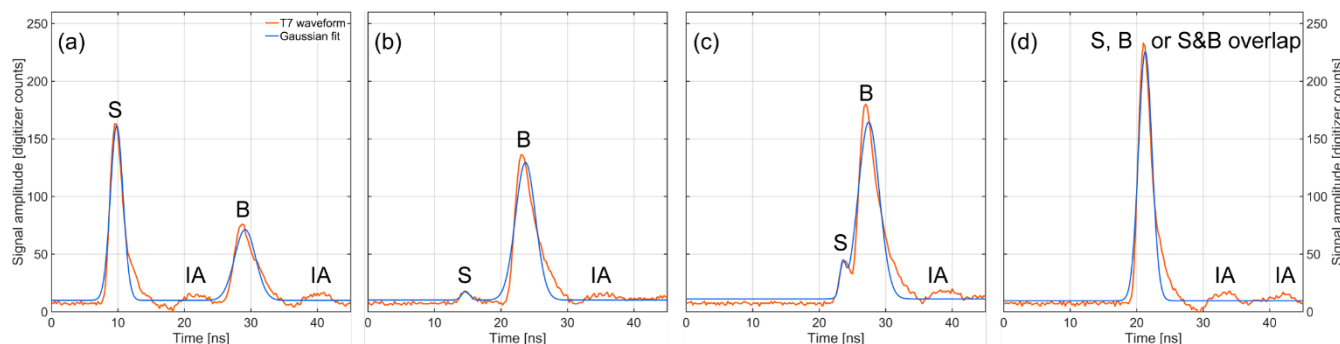
Figure 5: Example waveforms of lake return waveforms with Gaussian fits. S marks surface return, B marks bottom return and IA indicates false return pulses that are caused by instrument artifacts (Fig. A2).

170 We have evaluated the performance of the nonlinear regression and Gaussian tracker to accurately reproduce the two-way travel time difference as a function of signal-to-noise ratio and pulse separation (Appendix B). A sensitivity analysis of the nonlinear regression was performed by using the mean difference between a synthetic water depth and 250,000 nonlinear regressions over a range of water depth and determine a reliable detection threshold of 0.30 m for the minimum water depth that can be resolved with our approach and instrument system configuration (Fig. B2).

175 The first step in estimating water depth is to determine the elevation and geolocation of the lake surface return of each laser shot that is consistent with ATM's centroid-based surface elevation tracker used for the Level 1B data products. First, the uncalibrated slant range in air is determined from the two-way travel time difference between the transmit and receive pulse. Then, an intensity-dependent range walk calibration that is determined during ground test needs to be applied to the uncalibrated ranges to account for the combined effects of delay fibers and other system components on the range estimates.

180 Following that, a range correction needs to be applied to the range estimates due to the atmosphere affecting photon velocity. Scan azimuth and range bias corrections need to be applied as well. All required corrections are provided in the ATM waveform products. The ATM processing flow is detailed in Appendix B and documented in the MATLAB® code published with this paper (https://doi.org/10.5281/zenodo.6341229) (Studinger, 2022). The purpose of the approach presented here is not to produce absolute elevation measurements that are accurate and consistent within a campaign and between campaigns

185 but to reliably determine the water depth of supraglacial hydrological features.

Once the elevation and geolocation of the lake surface return have been determined the slant range in water and geolocation of the lake bottom returns are estimated while accounting for the refractive index of water in both geolocation and range. This is done by using Snell's law in vector form in geographic coordinates on the reference ellipsoid. The angle of incidence and geodetic azimuth of the lidar footprint on the lake surface, together with the lake surface elevation, the slant range in

190 water, and the refractive index in air and water determine the location and elevation of the lidar footprint on the lake bottom. For laser shots that only have a lake bottom return (e.g., Fig. 5d) the propagation in water needs to be properly accounted for. We first fit a plane through surrounding lake surface elevations and use the resulting elevation of the plane as mean lake surface elevation. We then calculate the intersection of the laser beam transmitted from the aircraft with the mean lake surface using the geodetic azimuth of the laser beam transmitted from the aircraft to the surface target, the off nadir pointing

195 angle and the location and elevation of the scan mirror/laser sensor (Fig. A3), which is the fiducial reference point for all two-way travel time estimates. Based on the location of the intersection the slant range and hypothetical two-way travel time between the scan mirror/laser sensor and the intersection of the laser beam with the lake surface can be calculated. Using the hypothetical lidar footprint on the lake surface, the proper location and elevation footprints of laser shots with only lake bottom returns can be calculated. A flow diagram summarizes the processing steps to derive geolocated water depth

200 estimates (Fig. B3).

5 Results and discussion

The primary purpose of this paper is algorithm and method development and therefore we discuss the bathymetry of only a few select hydrological features here. We have, however, applied the hydrological feature detection algorithm to the entire Spring 2019 data set in order to select those examples and begin with a discussion of the example selection and selection criteria.

5.1 Locations of supraglacial hydrological features identified in Spring 2019 data: results and discussion

We analyze all CAMBOT Level 0 images from flights between May 5, 2019 and May 16, 2019 that are below the approximate elevation cutoff for the equilibrium line and within the ice mask. The locations of images with $NDWI_{ice}$ exceeding the detection threshold are shown with blue circles in Fig. 6 for central west Greenland. As can be expected, that early in the melt season most of the hydrological features are located near the ice margin and at low elevations. Despite the earlier increase in air temperatures in southern Greenland, compared to central west Greenland and presumed longer exposure to surface melt conditions at the transition from Winter to Spring, we found no compelling evidence for liquid water along our flight lines in southern Greenland in the Spring 2019 data. A possible explanation for this is that the ice margin and location of our flight lines are at higher elevations in southern Greenland than they are in central west Greenland and therefore likely exposed to cooler temperatures (Fig. 2). This observation is consistent with the lakes farthest inland being observed in the Sermeq Kujalleq (Jakobshavn Isbræ) area near Ilulissat (Fig. 6) where the ice surface within the Sermeq Kujalleq drainage basin is at lower elevations (Fig. 2) and likely has experienced warmer air temperatures and therefore more melt days than the higher elevations farther south.

We have visually analyzed the images identified as having water surfaces and selected several features that we consider suitable for algorithm and method development. These include a variety of features such as lakes and streams, as well as varying conditions with thin lake ice and surface waves. Lidar data spatial coverage and the depth of lakes are additional criteria used for selection of the below examples. The next section will discuss water depth estimates of these select features.
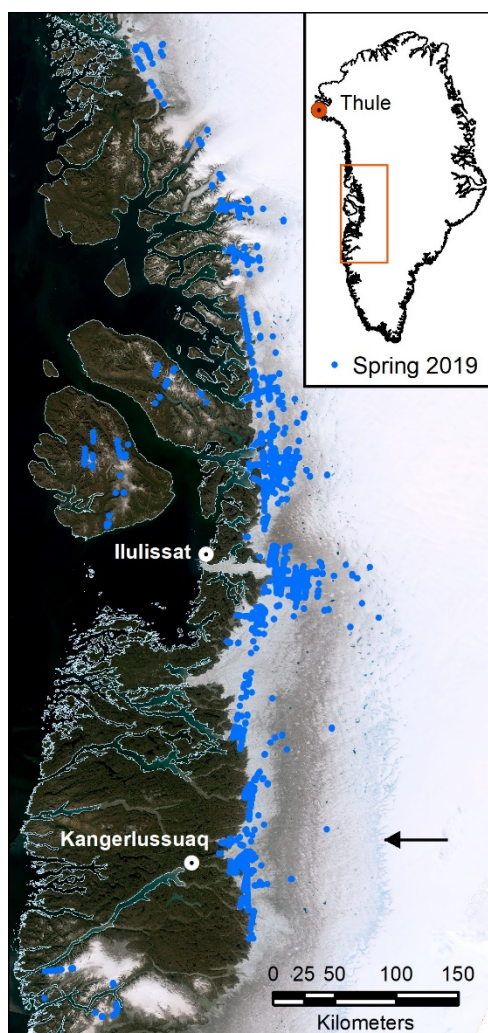
Figure 6: Locations of hydrological features in central west Greenland identified in Spring 2019 data (blue circles). Background image is a Sentinel-2 image mosaic from MacGregor et al. (2020) from August 2019. The approximate location of the transition between the ablation zone and the accumulation zone (equilibrium line) in August 2019 is indicated by the black arrow.

5.2 Depth estimates of supraglacial hydrological features: results and discussion

The first example, one of the deepest lakes we found, is approximately 140 m wide and 500 m long with complete lidar coverage and a smaller 140 × 40 m lake to the east with partial lidar coverage (Fig. 7). Prior to ATM data acquisition on May 6, 2019 the lake location itself had experienced 6 days of melt since the first recorded onset of melt on April 13, 2019 and 8 days of freezing since then (Fig. A1b). Meltwater that pools in both lakes also forms upstream but the extent of the catchment area is not known due to a lack of data upstream of the lidar swath. Figure 7a and b illustrate the much denser sampling and level of detail that can be derived from airborne measurements compared to spaceborne measurements. The ICESat-2 data closest in time and space over this lake was acquired on June 13, 2019, 38 days after the ATM pass. Inset map

A) in Fig. 7a shows clearly visible wind-induced waves on the surface of the lake, suggesting that the assumption of a lake surface without waves required for optical depth-based estimates might not be the case for many lakes (Sneed and Hamilton, 2011). Inset map B) in Fig. 7a shows shadows at the lake bottom from an ice floe at the surface. The length of the shadows could be used together with the elevation and azimuth of the sun at the time of data acquisition to independently estimate the
240 water depth at the edge of the shadow. However, we believe that lidar-based methods are more accurate, in particular since the freeboard of the ice floe is not known without lidar data.

The return signal strength (Fig. 7b) over the lakes and ponds is much weaker than over the snow and ice surfaces seen in the natural-color image mosaic (Fig. 7a) as expected. The return signal strength in Fig. 7b is from the Level 1B point cloud data products (ILATM1B and ILNSA1B, Tab. 1) and includes lake bottom returns. Furthermore, the wide and narrow scanners
245 are entirely independent lidars and therefore the absolute return signal strength differs as a result of instrument characteristics and instrument settings during data acquisition. Nevertheless, the correlation between water surfaces visible in the natural-color imagery and relative return signal strength of the lidar data is pronounced. The lower return signal strength also correlates well with $NDWI_{ice}$ calculated from natural-color CAMBOT images (Fig. 7b, c). This correlation is also the case for very small ponds marked by circles in Fig. 7b and c. The $NDWI_{ice}$ representation (Fig. 7c) reveals narrow melt water
250 channels connecting the lakes that are difficult to observe in both the natural color and return signal strength data (Fig. 7a, b). The mean lake surface elevation of the small lake east of the main lake is 30 cm above the lake surface of the main lake implying water from the small lake is flowing downhill into the main lake through the two channels visible in $NDWI_{ice}$ data marked by arrows (Fig. 7c).

We use the $NDWI_{ice}$ threshold algorithm described in Section 3 to assign a surface type (snow and ice, or water) to each lidar
255 footprint for further processing (Fig. 7d). Figure 7e shows the lidar footprint elevations that have been identified as being either over snow and ice or a water surface. The surface returns over the lake show gaps in the northwestern part of the main lake. The gaps are related to the angle of incidence: a combination of the aircraft's pitch and roll angle over the lake segment and resulted in a difference in angle of incidence of 9° between the northwestern and southeastern parts of the main lake with the southeastern lidar footprints closer to nadir and therefore more likely to trigger recording of a lake surface return. In
260 addition to the aircraft's pitch and roll angle, the geometry of a nutating mirror also results in differences of angles of incidence between forward and aft scan of around 2° with the aft scan being closer to nadir. With a flight direction from north to south, Fig. 7e shows that surface returns on the T6 wide scanner are mostly from aft scans as can be expected. The narrow scanner with a 2.5° off-nadir scan angle shows almost complete lake surface return coverage.

Figure 7f shows the water depth of the main lake, the small lake to the east, and some of the smaller supraglacial
265 hydrological features such as ponds and channels. Over the main lake, water depths gradually deepen from the shore towards the interior of the lake and reaching maximum depth of 7 m in narrow bottom crevasses (marked by arrows). The ability to resolve these crevasses through water depth measurements illustrates the level of detail that can be derived from airborne measurements. The gradual deepening from the shore to 7 m over the distance of approximately 70 m, suggests that the

assumption of a homogenous lake bottom that is roughly parallel to the lake surface used for optical depth-based estimates
270   must be used with caution (Sneed and Hamilton, 2011).
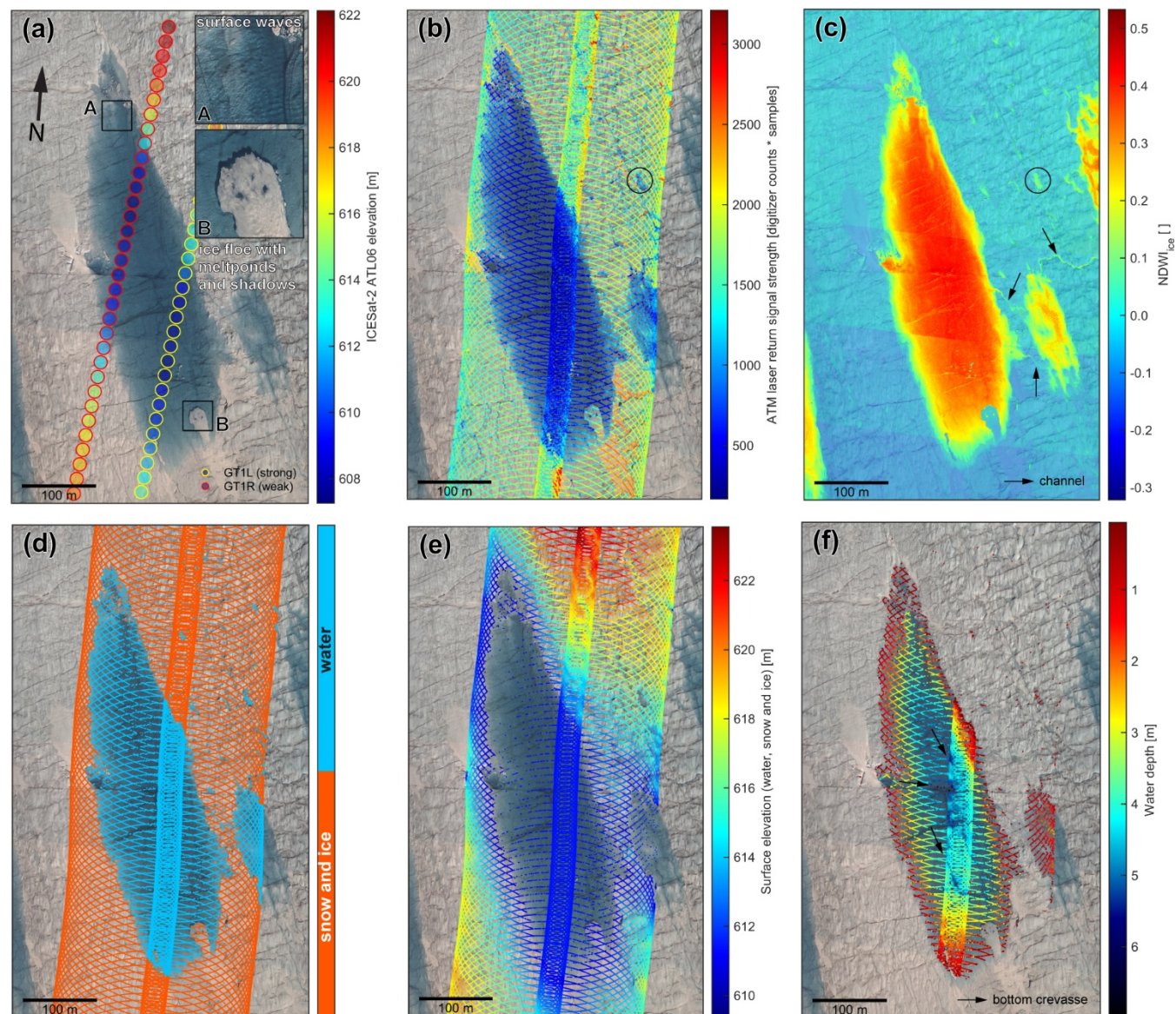
Figure 7: (a) Mosaic of 5 geolocated, orthorectified CAMBOT natural color (red, green, blue) images of a supraglacial lake. ICESat-2 data closest in time and space was acquired on June 13, 2019, 38 days after the ATM pass over the lake on May 6, 2019. **(b)** Return signal strength of the ATM T6 (wide scan) and T7 (narrow scan) laser footprints. The return signal strength is significantly lower over the lake
275   compared to the surrounding snow and ice surface. **(c)** NDWI$_{ice}$ plotted over CAMBOT image mosaic with NDWI$_{ice}$ pixels below the detection threshold of 0.05 shown at 50% opacity/transparency. **(d)** Surface classification of ATM laser footprints based on NDWI$_{ice}$ pixels using a classification threshold of 0.05. **(e)** Surface elevation of laser footprints over snow, ice and water. **(f)** Water depth of hydrological features. For location see Fig. 2. Surface temperature and surface melt indicator from MODIS (Hall et al., 2018; Hall and DiGirolamo, 2019) and the number of melt days for this location are shown in Fig. A1b.

280

The deeper water depths toward the interior of the main lake correlate with higher NDWI$_{ice}$ values (Fig. 7c, f). This change in spectral properties with water depth is used in optical depth-based estimates to derive water depths.
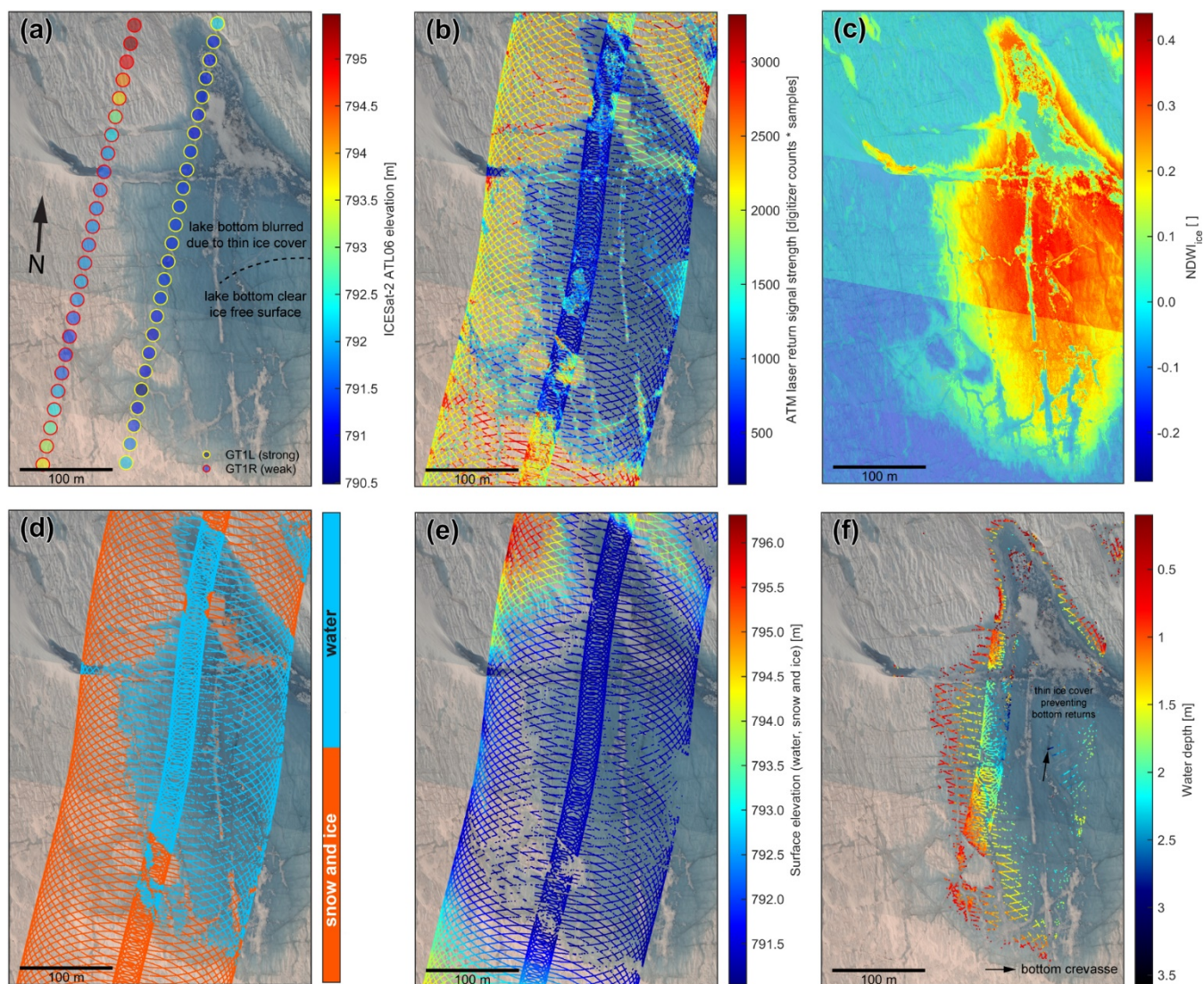
Figure 8: (a) Mosaic of 5 geolocated, orthorectified CAMBOT natural color images of a supraglacial lake. ICESat-2 data were acquired 3 hours after the ATM pass over the lake on May 15, 2019. **(b)** Return signal strength of the ATM T6 and T7 laser footprints. The return signal strength is significantly lower over the lake compared to the surrounding snow and ice surface. **(c)** NDWI$_{ice}$ plotted over CAMBOT image mosaic with NDWI$_{ice}$ pixels below the detection threshold of 0.05 shown at 50% opacity/transparency. **(d)** Surface classification of ATM laser footprints based on NDWI$_{ice}$ pixels using a classification threshold of 0.05. **(e)** Surface elevation of laser footprints over snow and ice. **(f)** Water depth of hydrological features. For location see Fig. 2. Surface temperature and surface melt indicator from MODIS (Hall et al., 2018; Hall and DiGirolamo, 2019) as well as number of melt days for this location are shown in Fig. A1c.

The second example (Fig. 8) is a lake with slightly different conditions than the first one. Between the day of the airborne survey on May 15, 2019, and the first reported occurrence of melt on April 29, 2019, this location had experienced 11 days

with melt and 6 days without melt (Fig. A1c). The airborne survey was a coordinated ICESat-2 under flight with airborne
295   data acquired just 3 hours before ICESat-2 passed over the lake. The lake contains several snow-covered patches of lake ice
that are obscuring the view of the lake bottom and prevent enough lidar light to reach the lake bottom necessary to trigger
recording of a bottom return pulse (Fig. 8a). Thin layers of lake ice impose limitations not only for airborne and spaceborne
lidar-based water depth estimates but also for any optical depth-based bathymetry estimates. The high-resolution natural
color imagery reveals relevant details that currently cannot be identified with spaceborne sensors. On the eastern side of the
300   lake there is a sharp transition in visibility of details such as crevasses and other structures on the lake bottom to a blurred
lake bottom north of it (Fig. 8a). While not discernible in the natural color imagery it is likely that the blurring of the lake
bottom is caused by a thin layer of clear lake ice. This thin ice cover also acts as a specular reflector for laser light and likely
reflects lidar energy away from the detector, thereby causing gaps in bottom returns. This interpretation is supported by the
weaker return signal strength over the area with thin ice cover compared to the ice-free water surface south of it (Fig. 8b).
305   Figure 8c shows some of the limitations of using a simple $NDWI_{ice}$ detection threshold for surface classification. When
exposure time between CAMBOT frames is either automatically or manually adjusted, the brightness of pixels and therefore
the $NDWI_{ice}$ value of the same feature changes from frame to frame, as can be seen in Fig. 8c. However, the visual
correlation with water surfaces in the natural color imagery (Fig. 8a), the lidar return signal strength (Fig. 8b), and the lidar
footprint surface classification (Fig. 8d) shows that an $NDWI_{ice}$ detection threshold is a robust surface classification method
310   for the purpose of this paper.

The water depth within this lake gradually deepens from its western shore towards the interior of the lake before becoming
shallower again. The deepest returns are around 3.5 m but most of the deepest part of the lake lack bottom returns. As can be
seen in Fig. 8e, the loss of bottom returns is not a simple function of water depth alone. Some of the deepest returns are
located within a narrow bottom crevasse (marked by an arrow in Fig. 8e) that has no returns in the shallower parts around it.
315   A possible explanation for this is that the slope of the sidewalls of the crevasse or channel is closer to the normal of the lidar
beam than in the surrounding areas and therefore lidar light is reflected back to the sensor on the aircraft. Also, concave-
shaped surfaces, such as found in crevasses and channels, can have a focusing effect that increases the intensity of the
reflected lidar light and increases the likelihood of exceeding the signal strength necessary to trigger recording of a bottom
return pulse.
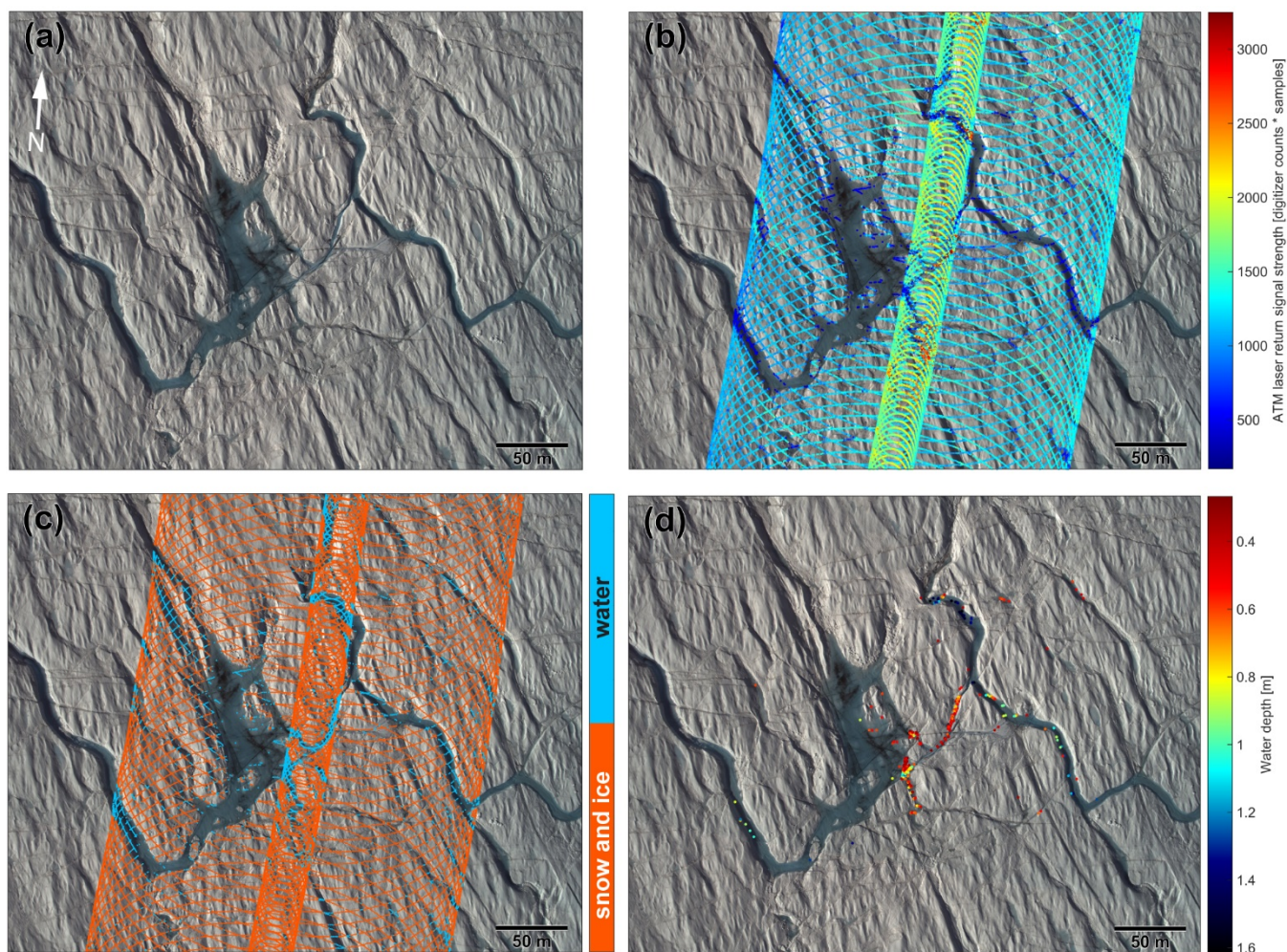
320
Figure 9: (a) Mosaic of 2 geolocated, orthorectified CAMBOT natural color images of a supraglacial lakes, streams, and channels from May 12, 2019. **(b)** Return signal strength of the ATM T6 and T7 laser footprints. **(c)** Surface classification of ATM laser footprints based on NDWI$_{ice}$ pixels using a classification threshold of 0.05. **(d)** Water depth of hydrological features. For location see Fig. 2. Surface temperature and surface melt indicator from MODIS (Hall et al., 2018; Hall and DiGirolamo, 2019) as well as number of melt days for this location are shown in Fig. A1d.

The third example shows a network of narrow, 5-10 meter wide, meltwater channels and streams and reflects the most challenging targets for bathymetric imaging found in this study (Fig. 9). Following the first reported melt between April 29, 2019 and the day of the airborne survey, this location had experienced 11 days of melt and 1 day of freezing (Fig. A1d). There are no ICESat-2 footprints within the extent of the data frame shown. In general, we find that channels and streams show a very low number of both surface and bottom returns compared to lakes (Fig. 9). A possible explanation is that these narrow streams flow in topographic channels that provide more protection from surface winds compared to relatively open lakes shown in Figs. 7 and 8. Wind protection hinders generation of surface capillary waves, which are necessary to reflect lidar energy back to the sensor on the aircraft. The presumably flat water surface of these streams acts a specular reflector

directing lidar energy away from the sensor and resulting in very few surface and bottom returns. The deepest returns of
340   around 1.6 m can be seen in a bend of a channel near the northern end of the data frame.

We compared pulse widths of lake surface and lake bottom return pulses of the hydrological features we have discussed, and
we found no relationship between pulse width and slant range in water potentially caused by volume scattering in water. In
addition to volume scattering in water the slope and roughness of the lake bottom will likely be bigger contributors to pulse
widening than volume scattering. The extremely clear water visible in true-color imagery suggests very low turbidity of
345   these water bodies, which in turn should result in very little volume scattering and associated pulse broadening.

6 Conclusions

ATM's suite of co-located sensors, small laser footprints (64 cm), high shot density, swath coverage, and high-resolution
imagery (10 cm) reveals fine-scale hydrological features, such as very narrow meltwater channels and surface waves that
cannot be detected from space. Airborne measurements can also image supraglacial hydrological features at a spatial scale
350   and coverage that cannot be achieved by local measurements from short-range drones, which are often operated out of
remote field camps and require line-of-sight communications. The accuracy and resolution from airborne measurements
compared to spaceborne sensors provides critical complementary information that can support calibration and validation of
spaceborne methods and provide information necessary for high-resolution process studies of the supraglacial hydrological
system on the GrIS that currently cannot be achieved from spaceborne observations alone. The minimum water depth that
355   can be resolved with the current algorithm using a 1.3 ns laser pulse sampled at 4 GHz is around 30 cm, and the maximum
water depth measured with the ATM optimized for snow and ice elevation measurement was around 7 meters. However, this
could also reflect the maximum water depth encountered early in the melt season rather than an instrument limitation.

Appendix A
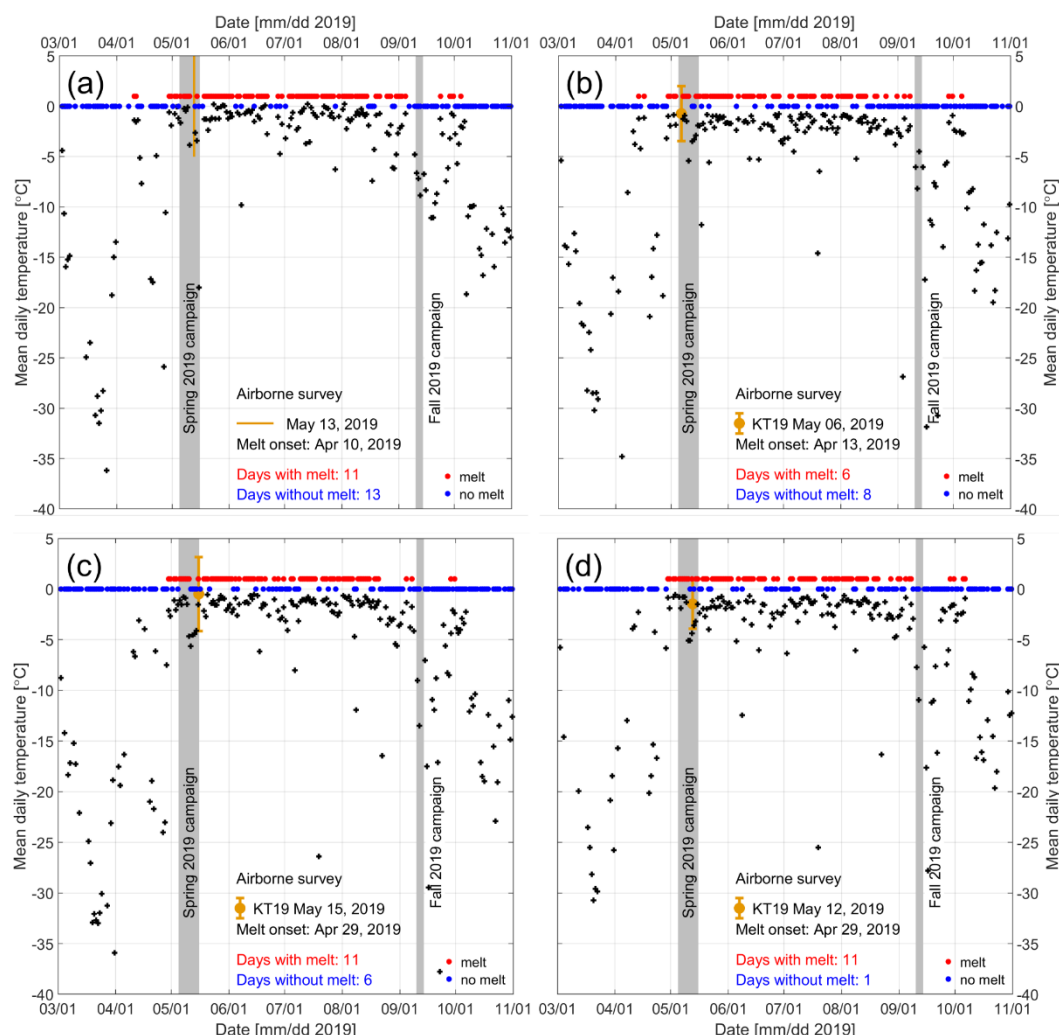
Figure A1: Surface temperature (black crosses) and surface melt indicator (red and blue circles) from MODIS (Hall et al., 2018; Hall and DiGirolamo, 2019) and mean ATM KT19 infrared surface temperatures (Studinger, 2019) averaged in 60 second windows over the hydrological features with 1-σ standard deviation. The windows of operation of the Spring and Fall 2019 campaigns are indicated by vertical gray areas in all panels. Panel a) show the times series for the approximate location of the oblique aerial photograph in Fig. 1, panel b) is for the lake shown in Fig. 7, panel c) is for the location of the lake shown in Fig. 8, and panel d) is for the location of the streams and channels shown in Fig. 9.

ATM KT19 infrared surface temperatures

The KT19 is an infrared radiation pyrometer that is used to measure infrared radiation wavelengths between 960 and 1150 nm that are used to derive skin temperatures within the field of view of the sensor. At a nominal flight elevation of 460 m AGL, the two-degree field of view of the sensor results in an approximately 15 m measurement footprint on the surface. Measurements are taken at 10 Hz (Studinger, 2019).
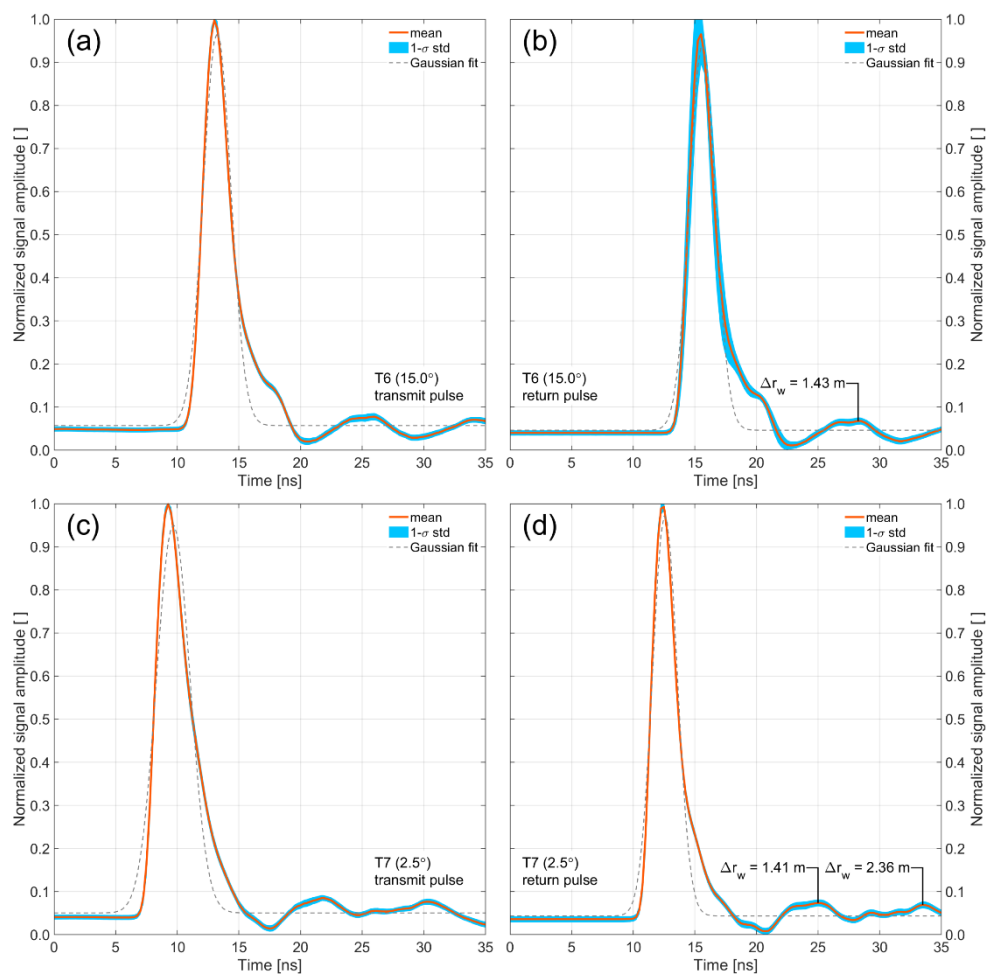
Figure A2: Averaged, normalized, unsaturated transmit and return waveforms of the T6 (top) and T7 (bottom) transceivers acquired over the airport ramp in Kangerlussuaq, Greenland on May 13, 2019. The impact of surface slope and surface roughness of the ramp's concrete surface within an ATM laser footprint do not contribute to the shape of the return waveform and can be neglected. The concrete surface has no subsurface penetration for 532 nm laser light. The main peak is followed by smaller artifact peaks, the first of which occurs 12.75 ns after the main peak in T6 and 12.5 ns in the T7 waveforms. The difference between T6 and T7 corresponds to 1 sample for a digitization rate of 4 GHz (0.25 ns). The second peak in T7 occurs 21 ns after the surface return. The corresponding slant range in water is Δr_w. All 3 peaks have an amplitude of 7% of the surface return. For T6 28084 waveforms were stacked and for T7 48703. The deviation from a Gaussian shape is the combined result of characteristics of the laser, photomultiplier detectors and various other system components such as optical delay fibers and are common in waveform data of airborne and spaceborne lidars (Fig. A3).
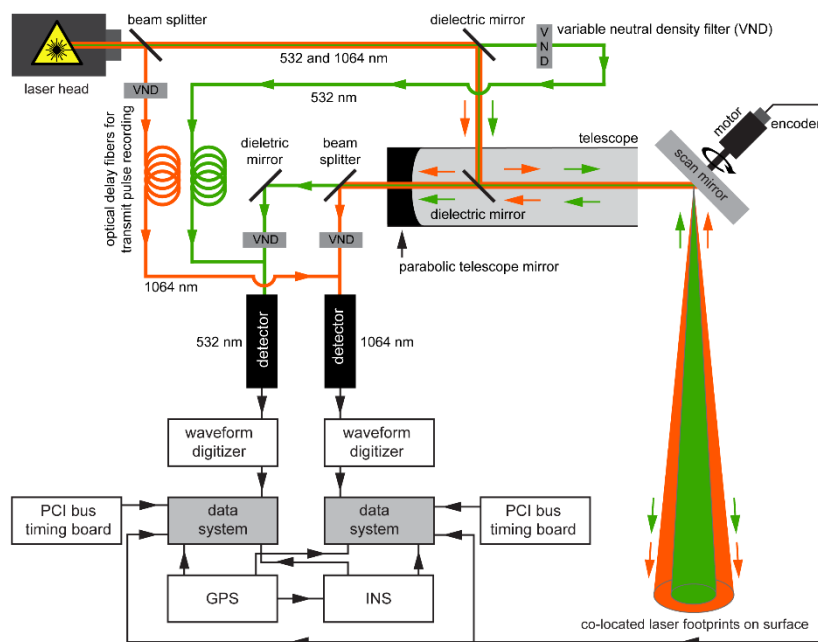
385

Figure A3: Schematic diagram of ATM's dual color T7 transceiver with co-located green (532 nm) and IR (1064 nm) footprints.

Appendix B

This section describes the processing flow for the ATM lidar data used in this paper for estimating surface elevations and water depths. The MATLAB® code is available at https://doi.org/10.5281/zenodo.6341229 (Studinger, 2022).

Geolocation of the laser sensor

The position of the Global Navigation Satellite System (GNSS) antenna on top of the fuselage of the survey aircraft is determined from NAVSTAR Global Positioning System (GPS) and Globalnaya Navigatsionnaya Sputnikovaya Sistema (GLONASS) carrier phase measurements recorded by receivers on the aircraft. These measurements are combined in post-flight processing with similar measurements from multiple static ground stations to determine a kinematic differential solution (DGPS) of the antenna trajectory. The lever arm from antenna to ATM scan mirror provided in the ATM waveform data products includes corrections for aircraft-specific changes in antenna phase centers that are determined for each campaign. The reference point for all lidar measurements is the scan mirror fiducial point (Fig. B2). To determine the location of the scan mirror/laser sensor in both space and time, the DGPS solutions are combined with aircraft attitude measurements from a commercial Inertial Navigation System (INS) on the survey aircraft, often also referred to as Inertial Measurement Unit (IMU), and measurements of the lever arm between the antenna and scan mirror in an aircraft-fixed cartesian coordinate system with the origin in the phase center of the antenna. The coordinate translations and rotations are done in a geocentric ECEF (Earth-centered, Earth-fixed) coordinate system, which are then converted to geographic coordinates for the position of the laser sensor.

Determination of time of flight and uncalibrated raw ranges using a centroid-based tracking algorithm

The two-way travel time difference Δt (i.e., the time of flight) is determined using the centroid of the transmit (t_{rx}) and receive (t_{rx}) pulses. The centroid t_c of a discrete waveform $w(t)$ is defined as:

$$t_c = \sum_{i=t_{start}}^{i=t_{end}} w(t_i) * t_i \left/ \sum_{i=t_{start}}^{i=t_{end}} w(t) \right.$$

$w(t)$ is the amplitude recorded by the waveform digitizer (in counts) minus the baseline, which is estimated from the median of the first 21 samples of the waveform. The ATM tracking algorithm used for the data presented in this paper uses 15% of the maximum amplitude above the baseline as a threshold to determine t_{start} by interpolating between samples. Similarly, t_{end} is defined as the first interpolated point where $w(t)$ falls below the 15% threshold. The uncalibrated range r_{uncal} between the two centroids of the transmit and receive pulse is:

$$r_{uncal} = \tfrac{1}{2} * c * (t_{rx} - t_{tx})$$

where *c* is the speed of light in vacuum.

Range calibration determined from ground calibration data

In pressurized aircraft the transmitted laser pulse travels thru the aircraft's optical window close to the scan mirror (Fig. A2).
Backscatter from both the scan mirror and the aircraft's optical window in the fuselage are close in time to the transmitted
425   laser pulse and partially overlap with the transmit waveform. To record a "clean" transmit waveform the transmit pulse is
sampled from behind a translucent beam splitter and subsequently injected into a multimode fiber-optic cable to provide a
fixed optical delay that results in temporal separation between the recorded transmit pulse and contamination from
backscattered photons from the scan mirror and the aircraft's optical window (Fig. A3). The optical delay fiber and other
system components introduce a laser time-of-flight range bias that needs to be determined from ground calibration
430   measurements.
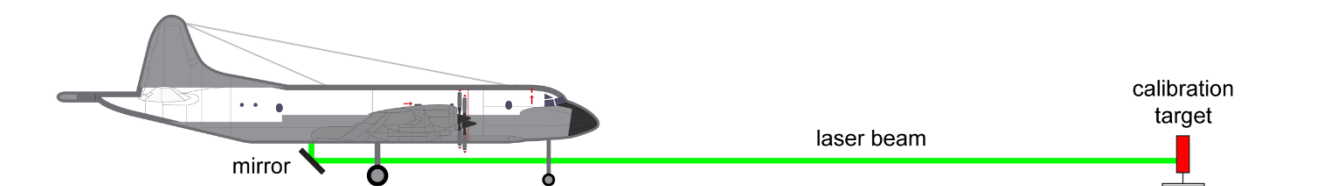
Figure B1: Range bias determination (a.k.a. ground test) using a calibration target with a known distance. The range to the calibration
target is measured with an electronic distance meter (a.k.a. "total station") with an accuracy of a few mm.

https://doi.org/10.5281/zenodo.6248436 (Studinger et al., 2022).

Determination of mounting biases

Martin et al. (2012) describe the process of estimating the 6 mounting biases related to range, scan angle, attitude and
position using ramp passes and cross-over analysis. Harpold et al. (2016) describe an alternative approach using the
445   difference between forward and aft scan elevations. These 6 biases are already applied to the data in the HDF5 waveform
files available from NSIDC.

Scan azimuth bias correction

Some campaigns contain scan-azimuth dependent elevation biases that can change over the course of a flight or a campaign. The elevation biases are a function of scan azimuth and are stored in `/mounting_parameters/scan_elv_adj`. The
450   elevation error due to azimuth error scales with the aircraft's elevation above ground level (AGL). It is determined for the nominal flight elevation (1500 ft/457 m). Scaling the correction with elevation is done by multiplying the aircraft's AGL with the elevation biases provided in the waveform data and dividing it by the nominal flight elevation (457 m). The resulting elevation-scaled values using `/mounting_parameters/scan_elv_adj` and `/aircraft/AGL` are subtracted from the elevation values. The lidar data from the Spring 2019 campaign used in this paper did not require scan azimuth bias
455   corrections.

Atmospheric range correction

The propagation speed of light is lower in a denser medium such as the atmosphere compared to vacuum. In laser altimetry this effect is referred to as atmospheric delay. The density of the atmosphere at the time and position of the aircraft and the footprint on the surface can be calculated from parameters provided by global numerical weather models. The density is
460   primarily a function of the temperature of air, the atmospheric pressure, and the partial pressure of water vapor and can be used to calculate the refractive index along the propagation path of a laser beam (Petrov, 2014). The range correction applied due to the atmosphere affecting photon velocity is provided in `/laser/atmos_cor` for each elevation measurement in the HDF5 waveform files and needs to be applied to the range estimates. The `/laser/atmos_cor` values are subtracted from the `/laser/calrng` slant ranges.

465   **Range bias**

The ultimate reference for in-flight data are the ramps, crossings, and along-track comparisons to produce consistent elevation measurements over the course of a campaign and between campaigns. Any residual bias thus determined (typically on the order of a few centimeters) is included in `/mounting_parameters/range_bias`, which are added to the range estimates (not elevation). The `/mounting_parameters/range_bias` is typically the same for an entire deployment but
470   can change when there was a hardware change (e.g., fiber swap, change fiber pickoff location) during a deployment.

Gaussian fit

The lake surface and lake bottom returns are fitted with a dual-peak Gaussian function $g_2(t)$ with 7 parameters:

$$g_2(t) = b + a_1 \, e^{-\frac{1}{2}\left(\frac{t-t_1}{\sigma_1}\right)^2} + a_2 \, e^{-\frac{1}{2}\left(\frac{t-t_2}{\sigma_2}\right)^2}$$

475

where b is the signal baseline (noise floor), $a_{1,2}$ are the pulse amplitudes, $t_{1,2}$ are the pulse locations of the pulse maxima and means, and $\sigma_{1,2}$ are the 1-sigma (1-σ) pulse widths. The nonlinear regression is done using initial values estimated using output from MATLAB®'s Signal Processing Toolbox `findpeaks` as input for MATLAB®'s Statistics and Machine Learning Toolbox `nlinfit` function.

480 **Sensitivity analysis:** The performance of the nonlinear regression to accurately reproduce the two-way travel time difference is a function of signal-to-noise ratio and pulse separation. For a 20 cm slant range in water the two-way travel time difference between the surface and bottom return pulses is 1.78 ns (Fig. B2a), which is close to the average pulse width of 1.63 ± 0.71 ns (1-σ)/ 3.84 ± 1.68 ns (FWHM) of the ATM T6 return laser pulse estimated from ground tests using a penetration-free target (Fig. B1). The average return pulse width of T7 is 1.20 ± 0.31 ns (1-σ)/ 2.82 ± 0.74 ns (FWHM). The

485 standard deviation (1-σ) of the baseline noise estimated from ground tests is 0.9 ± 0.1 digitizer samples for both T6 and T7. The minimum amplitude to trigger signal acquisition is 36 digitizer counts for both T6 and T7 resulting in a possible signal-to-noise ration range between 29:1 to 248:1 above the baseline for an 8-bit digitizer (7.0 ± 0.2 digitizer counts for T6 and 8.5 ± 0.5 digitizer counts for T7, respectively).
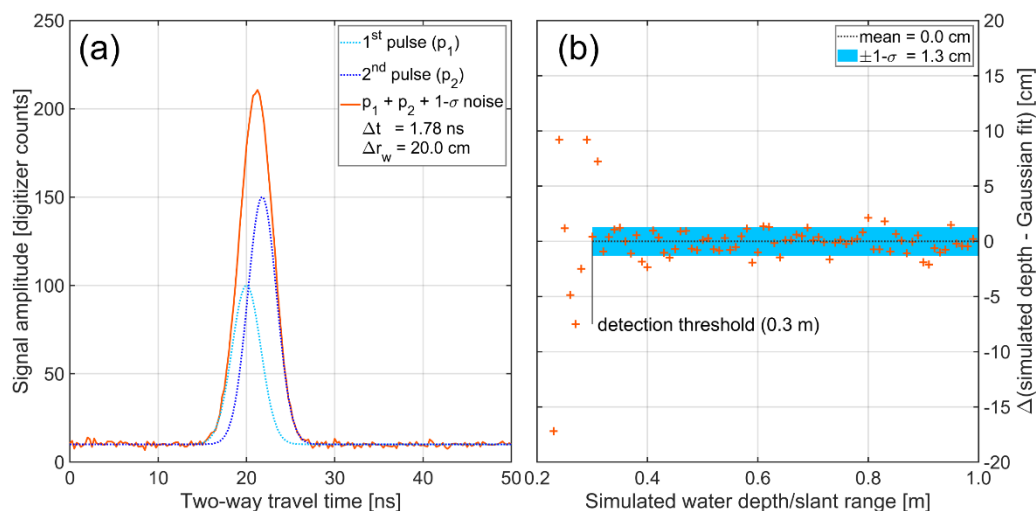
490

Figure B2: a) Synthetic Gaussian waveforms of overlapping surface and bottom return pulses. The FWHM pulse width is 1.6 ns (1-σ) and the mean of the two pulses is separated by $\Delta t = 1.78$ ns, which corresponds to a slant range $\Delta r_w = 20$ cm in water. The combined waveform has the average ATM T6 and T7 system noise level added. The two pulses are not discernible in the combined waveform. **b)** Sensitivity analysis of the nonlinear regression. The mean of difference between the synthetic water depth and the 250,000 nonlinear regressions for

495 each water depth is shown (orange crosses) and the standard deviation (1-σ) and mean for water depths greater than the detection threshold of 0.30 m are shown.
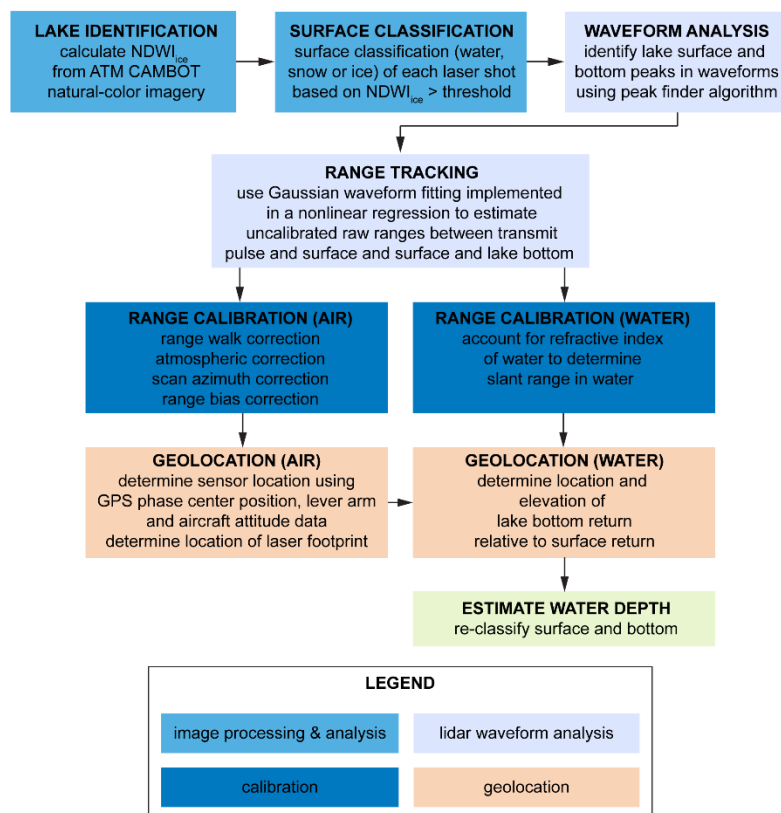
Figure B3: Flow diagram of the processing steps to derive geolocated water depth estimates.

Code availability. The MATLAB® code developed for this paper for tracking lake surface and lake bottom returns, analyzing
505 waveforms, geolocating ATM lidar footprints, and calculating water depths is available at
https://doi.org/10.5281/zenodo.6341229 (Studinger, 2022).
Chad Greene's MATLAB® function for interpolating GeoTIFF data is available on MATLAB®'s File Exchange website at:
https://www.mathworks.com/matlabcentral/fileexchange/47899-geotiffinterp.

510 *Data availability.* All ATM Operation IceBridge airborne data used in this study are freely available at the National Snow
and Ice Data Center at https://nsidc.org/icebridge/portal. The ATM waveform data from the two ground tests used here, the
true ranges and MATLAB® code for reading ground test data are available at: https://doi.org/10.5281/zenodo.6248436
(Studinger et al., 2022).

515 Greenland-wide topography and ice mask data are from the Greenland Ice Mapping Project (GIMP) Digital Elevation Model
(Howat et al., 2014) and (Morlighem, 2021, updated 2021) and are available at NSIDC at
https://nsidc.org/data/IDBMG4/versions/4.
The Sentinel-2 image mosaic from August 2019 from MacGregor et al. (2020) is available through QGreenland
at https://qgreenland.org/ or https://doi.org/10.5281/zenodo.5548326.
520 The ice surface temperature and ice surface melt indicator from MODIS (Hall et al., 2018; Hall and DiGirolamo, 2019) are
available at NSIDC at https://doi.org/10.5067/7THUWT9NMPDK.
The Sentinel-2A image used in Fig. 2 is available from the USGS EarthExplorer website at https://earthexplorer.usgs.gov/.

Author contributions. MS led the analysis of the laser altimetry, optical imagery, integration of results and prepared the
525 manuscript. All authors helped interpret the analysis, develop the methods and comment on the manuscript.

Competing interests. The authors declare that they have no conflict of interests.

Acknowledgements. This paper reflects the combined efforts of all ATM team members over many decades of instrument
530 development and field deployments. Jeremy Harbeck and Nathan Kurtz are thanked for developing the ATM CAMBOT
L1B Version 2 data product. We thank the Operation IceBridge flight crews that made data collection for this study possible.

Financial support. This work was funded by NASA's Internal Scientist Funding Model and the Airborne Science Program.

535

References

Box, J. E., and Ski, K.: Remote sounding of Greenland supraglacial melt lakes: implications for subglacial hydraulics, Journal of Glaciology, 53, 257-265, 10.3189/172756507782202883, 2007.

540 Chu, V. W.: Greenland ice sheet hydrology:A review, Progress in Physical Geography: Earth and Environment, 38, 19-54, 10.1177/0309133313507075, 2014.

Corr, D., Leeson, A., McMillan, M., Zhang, C., and Barnes, T.: An inventory of supraglacial lakes and channels across the West Antarctic Ice Sheet, Earth Syst. Sci. Data, 14, 209-228, 10.5194/essd-14-209-2022, 2022.

Das, S. B., Joughin, I., Behn, M. D., Howat, I. M., King, M. A., Lizarralde, D., and Bhatia, M. P.: Fracture Propagation to

545 the Base of the Greenland Ice Sheet During Supraglacial Lake Drainage, Science, 320, 778-781, 10.1126/science.1153360, 2008.

Datta, R. T., and Wouters, B.: Supraglacial lake bathymetry automatically derived from ICESat-2 constraining lake depth estimates from multi-source satellite imagery, The Cryosphere, 15, 5115-5132, 10.5194/tc-15-5115-2021, 2021.

Enderlin, E. M., Howat, I. M., Jeong, S., Noh, M.-J., van Angelen, J. H., and van den Broeke, M. R.: An improved mass

550 budget for the Greenland ice sheet, Geophysical Research Letters, 41, 866-872, 10.1002/2013gl059010, 2014.

Fair, Z., Flanner, M., Brunt, K. M., Fricker, H. A., and Gardner, A.: Using ICESat-2 and Operation IceBridge altimetry for supraglacial lake depth retrievals, The Cryosphere, 14, 4253-4263, 10.5194/tc-14-4253-2020, 2020.

Flowers, G. E.: Hydrology and the future of the Greenland Ice Sheet, Nature Communications, 9, 2729, 10.1038/s41467-018-05002-0, 2018.

555 Hall, D. K., Cullather, R. I., DiGirolamo, N. E., Comiso, J. C., Medley, B. C., and Nowicki, S. M.: A Multilayer Surface Temperature, Surface Albedo, and Water Vapor Product of Greenland from MODIS, Remote Sensing, 10, 555, 2018.

Hall, D. K., and DiGirolamo, N. E.: Multilayer Greenland Ice Surface Temperature, Surface Albedo, and Water Vapor from MODIS, Version 1.: National Snow and Ice Data Center Distributed Active Archive Center: https://doi.org/10.5067/7THUWT9NMPDK: 2019

560 Harpold, R., Yungel, J., Linkswiler, M., and Studinger, M.: Intra-scan intersection method for the determination of pointing biases of an airborne altimeter, International Journal of Remote Sensing, 37, 648-668, 10.1080/01431161.2015.1137989, 2016.

Howat, I. M., Negrete, A., and Smith, B. E.: The Greenland Ice Mapping Project (GIMP) land classification and surface elevation data sets, The Cryosphere, 8, 1509-1518, 10.5194/tc-8-1509-2014, 2014.

565 Krabill, W. B., Abdalati, W., Frederick, E. B., Manizade, S. S., Martin, C. F., Sonntag, J. G., Swift, R. N., Thomas, R. H., and Yungel, J. G.: Aircraft laser altimetry measurement of elevation changes of the greenland ice sheet: technique and accuracy assessment, Journal of Geodynamics, 34, 357-376, 10.1016/s0264-3707(02)00040-6, 2002.

Legleiter, C. J., Tedesco, M., Smith, L. C., Behar, A. E., and Overstreet, B. T.: Mapping the bathymetry of supraglacial lakes and streams on the Greenland ice sheet using field measurements and high-resolution satellite images, The Cryosphere,

570 8, 215-228, 10.5194/tc-8-215-2014, 2014.

MacGregor, J. A., Fahnestock, M. A., Colgan, W. T., Larsen, N. K., Kjeldsen, K. K., and Welker, J. M.: The age of surface-exposed ice along the northern margin of the Greenland Ice Sheet, Journal of Glaciology, 66, 667-684, 10.1017/jog.2020.62, 2020.

575 MacGregor, J. A., Boisvert, L. N., Medley, B., Petty, A. A., Harbeck, J. P., Bell, R. E., Blair, J. B., Blanchard-Wrigglesworth, E., Buckley, E. M., Christoffersen, M. S., Cochran, J. R., Csathó, B. M., De Marco, E. L., Dominguez, R. T., Fahnestock, M. A., Farrell, S. L., Gogineni, S. P., Greenbaum, J. S., Hansen, C. M., Hofton, M. A., Holt, J. W., Jezek, K. C., Koenig, L. S., Kurtz, N. T., Kwok, R., Larsen, C. F., Leuschen, C. J., Locke, C. D., Manizade, S. S., Martin, S., Neumann, T. A., Nowicki, S. M. J., Paden, J. D., Richter-Menge, J. A., Rignot, E. J., Rodríguez-Morales, F., Siegfried, M. R., Smith, B. E., Sonntag, J. G., Studinger, M., Tinto, K. J., Truffer, M., Wagner, T. P., Woods, J. E., Young, D. A.,
580 and Yungel, J. K.: The scientific legacy of NASA's Operation IceBridge, Reviews of Geophysics, n/a, e2020RG000712, https://doi.org/10.1029/2020RG000712, 2021.

Martin, C. F., Krabill, W. B., Manizade, S. S., Russell, R. L., Sonntag, J. G., Swift, R. N., and Yungel, J. K.: Airborne Topographic Mapper Calibration Procedures and Accuracy Assessment 2012.

Morlighem, M. e. a.: IceBridge BedMachine Greenland, Version 4.: NASA National Snow and Ice Data Center Distributed
585 Active Archive Center: https://doi.org/10.5067/VLJ5YXKCNGXO: 2021, updated 2021

Nienow, P. W., Sole, A. J., Slater, D. A., and Cowton, T. R.: Recent Advances in Our Understanding of the Role of Meltwater in the Greenland Ice Sheet System, Current Climate Change Reports, 3, 330-344, 10.1007/s40641-017-0083-9, 2017.

Pitcher, L. H., and Smith, L. C.: Supraglacial Streams and Rivers, Annual Review of Earth and Planetary Sciences, 47, 421-
590 452, 10.1146/annurev-earth-053018-060212, 2019.

Pope, A., Scambos, T. A., Moussavi, M., Tedesco, M., Willis, M., Shean, D., and Grigsby, S.: Estimating supraglacial lake depth in West Greenland using Landsat 8 and comparison with other multispectral methods, The Cryosphere, 10, 15-27, 10.5194/tc-10-15-2016, 2016.

Smith, L. C., Chu, V. W., Yang, K., Gleason, C. J., Pitcher, L. H., Rennermalm, A. K., Legleiter, C. J., Behar, A. E.,
595 Overstreet, B. T., Moustafa, S. E., Tedesco, M., Forster, R. R., LeWinter, A. L., Finnegan, D. C., Sheng, Y., and Balog, J.: Efficient meltwater drainage through supraglacial streams and rivers on the southwest Greenland ice sheet, Proceedings of the National Academy of Sciences, 112, 1001-1006, 10.1073/pnas.1413024112, 2015.

Smith, L. C., Yang, K., Pitcher, L. H., Overstreet, B. T., Chu, V. W., Rennermalm, Å. K., Ryan, J. C., Cooper, M. G., Gleason, C. J., Tedesco, M., Jeyaratnam, J., van As, D., van den Broeke, M. R., van de Berg, W. J., Noël, B., Langen, P.
600 L., Cullather, R. I., Zhao, B., Willis, M. J., Hubbard, A., Box, J. E., Jenner, B. A., and Behar, A. E.: Direct measurements of meltwater runoff on the Greenland ice sheet surface, Proceedings of the National Academy of Sciences, 114, E10622-E10631, 10.1073/pnas.1707743114, 2017.

Sneed, W. A., and Hamilton, G. S.: Evolution of melt pond volume on the surface of the Greenland Ice Sheet, Geophysical Research Letters, 34, https://doi.org/10.1029/2006GL028697, 2007.

605 Sneed, W. A., and Hamilton, G. S.: Validation of a method for determining the depth of glacial melt ponds using satellite imagery, Annals of Glaciology, 52, 15-22, 10.3189/172756411799096240, 2011.

Studinger, M.: IceBridge ATM L1B Elevation and Return Strength with Waveforms, Version 1: NASA National Snow and Ice Data Center Distributed Active Archive Center: https://doi.org/10.5067/EZQ5U3R3XWBS: 2018, updated 2020

Studinger, M.: IceBridge KT19 IR Surface Temperature, Version 2. [2019]. Boulder, Colorado USA. NASA National Snow
610 and Ice Data Center Distributed Active Archive Center. doi: https://doi.org/10.5067/UHE07J35I3NB. Last accessed 2022: NASA National Snow and Ice Data Center Distributed Active Archive Center: 2019

Studinger, M., and Harbeck, J. P.: IceBridge CAMBOT L1B Geolocated Images, Version 2: NASA National Snow and Ice Data Center Distributed Active Archive Center: https://doi.org/10.5067/B0HL940D452L: 2019

Studinger, M., and Harbeck, J. P.: IceBridge CAMBOT L0 Raw Imagery, Version 1: NASA National Snow and Ice Data
615 Center Distributed Active Archive Center: https://doi.org/10.5067/IOJH8A5F48J5: 2020

Studinger, M., Medley, B. C., Brunt, K. M., Casey, K. A., Kurtz, N. T., Manizade, S. S., Neumann, T. A., and Overly, T. B.: Temporal and spatial variability in surface roughness and accumulation rate around 88° S from repeat airborne geophysical surveys, The Cryosphere, 14, 3287-3308, 10.5194/tc-14-3287-2020, 2020.

Studinger, M., Manizade, S., Linkswiler, M., and Yungel, J.: NASA's Airborne Topographic Mapper (ATM) ground
620 calibration data for the Arctic Spring campaign 2019: Zenodo: https://doi.org/10.5281/zenodo.6248436: 2022

Tedesco, M., and Steiner, N.: In-situ multispectral and bathymetric measurements over a supraglacial lake in western Greenland using a remotely controlled watercraft, The Cryosphere, 5, 445-452, 10.5194/tc-5-445-2011, 2011.

van den Broeke, M. R., Enderlin, E. M., Howat, I. M., Kuipers Munneke, P., Noël, B. P. Y., van de Berg, W. J., van Meijgaard, E., and Wouters, B.: On the recent contribution of the Greenland ice sheet to sea level change, The
625 Cryosphere, 10, 1933-1946, 10.5194/tc-10-1933-2016, 2016.

Yang, K., and Smith, L. C.: Supraglacial Streams on the Greenland Ice Sheet Delineated From Combined Spectral–Shape Information in High-Resolution Satellite Imagery, IEEE Geosci. Remote Sens. Lett., 10, 801-805, 10.1109/LGRS.2012.2224316, 2013.

Yang, K., and Smith, L. C.: Internally drained catchments dominate supraglacial hydrology of the southwest Greenland Ice
630 Sheet, Journal of Geophysical Research: Earth Surface, 121, 1891-1910, https://doi.org/10.1002/2016JF003927, 2016.

Yang, K., Karlstrom, L., Smith, L. C., and Li, M.: Automated High-Resolution Satellite Image Registration Using Supraglacial Rivers on the Greenland Ice Sheet, IEEE Journal of Selected Topics in Applied Earth Observations and Remote Sensing, 10, 845-856, 10.1109/JSTARS.2016.2617822, 2017.